



Cite this: *RSC Adv.*, 2021, **11**, 26832

## Characterization of pruned tea branch biochar and the mechanisms underlying its adsorption for cadmium in aqueous solution†

Chuan Han,<sup>a</sup> Miao Fei Wang,<sup>a</sup> Yanfang Ren,<sup>\*ab</sup> Liming Zhang,<sup>a</sup> Yu Ji,<sup>a</sup> Wenjia Zhu,<sup>a</sup> Yaping Song<sup>a</sup> and Junyu He<sup>ID \*ab</sup>

In the present study, discarded pruned tea branch was used to prepare a new biochar, and the physicochemical properties and adsorption characteristics were investigated by characterization and batch experiments. With increasing pyrolysis temperature from 400 to 800 °C, the yield, specific surface area, and acidic functional groups had significant differences. The optimum adsorption conditions were determined as pH = 6 and dosage of 2 g L<sup>-1</sup>. The pseudo-second-order kinetic and Langmuir isothermal model could fit well to the adsorption data, which showed that the adsorption process was dominated by monolayer chemical adsorption. The highest adsorption property (74.04 mg g<sup>-1</sup>) was obtained by the pyrolysis of tea branch biochar (TBB) at 700 °C owing to the adsorption mechanisms, including surface complexation, precipitation, metal ion exchange, and Cd<sup>2+</sup>–π interaction. After five cycles of desorption, biochar still showed superior adsorption (80%). Hence, the TBB acted as a regenerable adsorbent for treating Cd<sup>2+</sup>-containing wastewater.

Received 1st June 2021  
 Accepted 23rd July 2021

DOI: 10.1039/d1ra04235a  
[rsc.li/rsc-advances](http://rsc.li/rsc-advances)

### 1. Introduction

Heavy metal pollution has always been the main driving factor of aquatic environmental pollution.<sup>1</sup> Cadmium (Cd) is one of the heavy metals commonly used in industries, such as metallurgy, electroplating, electronics, and especially battery.<sup>2</sup> A large amount of effluent containing Cd<sup>2+</sup> is discharged into streams, lakes, and other water bodies with the rapid development of industrialization, which may result in serious pollution to water systems without proper treatment.<sup>3</sup> Due to its high fluidity, durability, and high toxicity, it easily builds up in the aquatic environment and eventually enters the human body through the food chain, which seriously endangers human health.<sup>4</sup> Consequently, it is significant to remove Cd<sup>2+</sup> effectively and easily from wastewater to ensure water quality and human health, before discharge to the water environment.

Currently, various remediation techniques for removing Cd<sup>2+</sup> from wastewater have been reported, including electrochemical, chemical precipitation, membrane separation, ion exchange, etc.<sup>4</sup> Nevertheless, the current techniques are limited by complex technical processes, high operating costs, high

energy consumption, or are unsuitable for the treatment of low concentration heavy metal wastewater.<sup>5</sup> Compared to the above methods, adsorption has the advantages of being economical, high efficiency, ease of operation, no secondary pollution, and low sensitivity to toxic substances and is regarded as a promising and environmentally friendly wastewater treatment method.<sup>6</sup> It is urgent to find highly efficient and low-cost adsorbents in large-scale implementation of Cd<sup>2+</sup> removal processes. As an environmental functional adsorbent, biochar has been considered for its environmental friendliness recently.

Biochar is a carbon-rich and stable byproduct of biomass pyrolysis under anoxic conditions. It can be made from various raw materials, including livestock waste, sludge, forestry and agricultural waste, and other organic materials.<sup>4,7,8</sup> Biochar has excellent physicochemical properties, including large specific surface area, unique pore structure, abundant surface functional groups, and high surface negative charge and charge density.<sup>9</sup> These remarkable characteristics make it play a vital role as an efficient and cheap adsorbent in the treatment of heavy metal pollution in water. Several studies have explored the removal of Cd<sup>2+</sup> by biochar in aqueous solutions.<sup>10–12</sup> Furthermore, to increase the biochar adsorption capacity for heavy metals, modification with chemical reagents, such as acid, bases, and KMnO<sub>4</sub>, has been widely used to prepare activated carbon. The ability of activated carbon as an adsorbent is caused by the increased surface area, changed porous structure, and improved surface functional groups and their amount on the carbon surface.<sup>13–15</sup>

<sup>a</sup>School of Environmental and Safety Engineering, Changzhou University, Changzhou, 213164, PR China. E-mail: [junyuhe0303@126.com](mailto:junyuhe0303@126.com); [yanfangren@126.com](mailto:yanfangren@126.com); Fax: +86 519 86330086; Tel: +86 519 86330086

<sup>b</sup>Jiangsu Petrochemical Safety and Environmental Engineering Research Center, Changzhou, 213164, PR China

† Electronic supplementary information (ESI) available. See DOI: [10.1039/d1ra04235a](https://doi.org/10.1039/d1ra04235a)



$\text{Cd}^{2+}$  sorption by biochar is a complex process as heavy metals are removed *via* different mechanisms.<sup>16</sup> Jia and Thomas found that the adsorption of  $\text{Cd}^{2+}$  by biochar involves cation exchange.<sup>17</sup> Teng *et al.* found surface complexation and coprecipitation were the primary contributors to the  $\text{Cd}^{2+}$  sorption process for pinecone biochar.<sup>18</sup> Ion exchange and precipitation were found as the dominant  $\text{Cd}^{2+}$  adsorption mechanisms on rice-husk biochar.<sup>19</sup> Wang *et al.* found that coordination of  $\text{Cd}^{2+}$  with  $\pi$ -electrons contributed to  $\text{Cd}^{2+}$  adsorption aqueous solutions.<sup>20</sup>

China is the largest tea-producing country in the world. There are over  $3.06 \times 10^6 \text{ hm}^2$  of tea plantations in China. Tea pruning is a key technology to cultivate tree crowns, renew and rejuvenate tree vigor. About 1 million tons of pruned tea branches (TB) are produced annually. Currently, most of the TB waste is burned or discarded, which not only pollutes the environment but also wastes a large amount of potential biomass resources. Therefore, the conversion of discarded biomass into high-value biological products is a subject worthy of study. However, there is no research on the production of biochar from TB and its application in the removal of  $\text{Cd}^{2+}$  from wastewater. Using TB waste to prepare biochar to adsorb  $\text{Cd}^{2+}$  in an aqueous solution can not only reduce the economic and environmental burden but also can be used for pollution remediation and effective utilization of agricultural waste.

The objective of the present study was to explore (1) the physicochemical properties of biochar prepared from TB at diverse pyrolysis temperatures, (2) the adsorption characteristics of  $\text{Cd}^{2+}$  on TBB at diverse pyrolysis temperatures, and (3) the adsorption mechanisms of  $\text{Cd}^{2+}$  on TBB. The results indicated that the biochar prepared from TB could be used as an adsorbent to replace the current adsorption materials.

## 2. Materials and methods

### 2.1 Feedstocks

Pruned tea branches were collected from the Longchi Mountain tea plantation in Yixing, Jiangsu Province, China. The TB was washed with deionized water, dried at  $85^\circ\text{C}$  in the oven until a constant weight was obtained, and then crushed by a pulverizer and sieved through a 20 mesh sieve. The powder was packed in sealed bags and stored in a desiccator at room temperature for further experiments.

### 2.2 Preparation of the biochar

30 g of TB powder was pyrolyzed in a tubular furnace (OTF-1200X, Kejing, China) with a gas flow rate of  $60 \text{ mL min}^{-1}$  in  $\text{N}_2$  atmosphere. The sample was heated to the carbonization temperature at the rate of  $10^\circ\text{C min}^{-1}$  and pyrolyzed at  $400^\circ\text{C}$ ,  $500^\circ\text{C}$ ,  $600^\circ\text{C}$ ,  $700^\circ\text{C}$ , and  $800^\circ\text{C}$ . After the carbonization for 2 h, it was cooled to room temperature, treated with 1 M HCl to remove ash, washed to neutral with deionized water, filtered, and dried at  $85^\circ\text{C}$  to constant weight. Subsequently, the TBB was ground and sieved through a 100 mesh sieve and kept in reserve in a sealed bag for characterization and batch experiments. Based on the heated temperatures, the biochar samples

were designated as TBB400, TBB500, TBB600, TBB700, and TBB800.

### 2.3 Characterization of the biochar

TBB ash contents were determined by muffle furnace heating at  $800^\circ\text{C}$  for 4 h. The mineral elemental compositions of TBB were measured by ICP-OES (Vista-AX, VARIAN, USA). The pH value of 1 : 20 (w/v) suspension was determined using a pH meter (FE28, Mettler-Toledo, Switzerland). Elements C, H, N, and O in TBB were measured using the elemental analyzer (CE-400, EA, USA). The thermal stability of TB and TBB were tested using thermal gravimetric analysis (TGA8000, PerkinElmer, USA) under an  $\text{N}_2$  atmosphere, and the temperature range was  $30$ – $950^\circ\text{C}$  at the rate of  $10^\circ\text{C min}^{-1}$ . The hemicellulose, cellulose, lignin, and extractive contents in TBB were estimated according to Lee *et al.*<sup>21</sup> The structure, surface morphology, and elemental mapping of TBB were captured by a scanning electron microscope (FE-SEM, EVO MA 25, Karl Zeiss, Germany). The specific surface area and pore structure of TBB were determined using a specific surface area pore analyzer (ASAP2020, micrometrics, USA) and Brunauer–Emmett–Teller (BET) method using the Rouquerol criterion.<sup>22</sup> Fourier Transform Infrared (FTIR-6300, JASCO, Japan) and X-ray photoelectron spectroscopy (XPS, Kratos, Shimadzu, Japan) were used to determine the types and contents of functional groups. X-ray diffraction (XRD, QC3, Jordan Valley, Israel) was used to analyze the crystalline structure of biochar. The  $\text{Cd}^{2+}$  content was determined using flame Atomic Absorption Spectrophotometer (AAS, aa-300, PerkinElmer Ltd, USA).

### 2.4 $\text{Cd}^{2+}$ sorption by biochar

Cadmium chloride ( $\text{CdCl}_2 \cdot 2.5\text{H}_2\text{O}$ ) was dissolved in 0.01 M  $\text{Ca}(\text{NO}_3)_2$  solution as background electrolyte to prepare  $1000 \text{ mg L}^{-1}$   $\text{Cd}^{2+}$  stock solution, which was diluted to the desired concentration. The pH of the initial solution of  $\text{Cd}^{2+}$  was adjusted with 0.1 M hydrochloric acid or sodium hydroxide solution. Batch experiments were carried out by adding 0.05 g TBB to 25 mL solutions containing initial  $\text{Cd}^{2+}$  concentration ( $100 \text{ mg L}^{-1}$ , pH 6) at constant temperature ( $25 \pm 0.5^\circ\text{C}$ ) and shaking at 200 rpm for 24 h unless specified otherwise. All the experiments were conducted in triplicate.

**2.4.1 Effects of dosage and initial pH.** Different dosages of TBB (1, 2, 5, 10, and  $20 \text{ g L}^{-1}$ ) were put in polyethylene centrifuge tubes containing  $\text{Cd}^{2+}$  solution. At the dosage of  $2 \text{ g L}^{-1}$ , the effect of initial pH in the range of 2–8 on the adsorption of  $\text{Cd}^{2+}$  was investigated. The final suspension was centrifuged at 10 000 rpm for 10 min, and the supernatant was filtered through a  $0.45 \mu\text{m}$  filter membrane. The concentration of  $\text{Cd}^{2+}$  in the filtrate was determined by AAS.

**2.4.2 Adsorption kinetics and isotherm analysis.** To assess the adsorption kinetics, TBB and  $\text{Cd}^{2+}$  solution (w/v = 1 : 500) were mixed and vibrated at a constant temperature. Samples were taken out at 5 min, 10 min, 0.25 h, 0.5 h, 1 h, 2 h, 4 h, 8 h, 12 h, and 24 h. The adsorption isotherms of  $\text{Cd}^{2+}$  on TBB were explored by adding the sample to different concentrations of

$\text{Cd}^{2+}$  solution ( $10\text{--}300 \text{ mg L}^{-1}$ ). The  $\text{Cd}^{2+}$  concentration in the filtrate was filtered and determined by the above method.

Adsorption of  $\text{Cd}^{2+}$  onto TBB was evaluated by adsorption kinetic models (pseudo-first order,<sup>23</sup> pseudo-second order, and Elovich models) and isotherm models (Langmuir, Freundlich, and Temkin models) (additional information available in ESI†).

## 2.5 Reusability potential of biochar

The reusability potential of biochar was determined by desorption experiments. 0.05 g  $\text{Cd}^{2+}$  saturated TBB700 was mixed with 25 mL 0.01, 0.1, and 1 M  $\text{HCl}$ ,  $\text{HNO}_3$ , and  $\text{H}_2\text{SO}_4$ , respectively, and shaken continuously for 24 h at  $25 \pm 0.5^\circ\text{C}$  and 200 rpm. The desorption efficiency of  $\text{Cd}^{2+}$  was tested to determine the optimal desorption conditions. The TBB700 desorbed under the optimal desorption condition in the previous step was washed and dried again for the adsorption test. The continuous desorption–adsorption cycle was repeated five times to test the reusability of TBB.

## 3. Results and discussion

### 3.1 Biochar yield

As the temperature increased, the yield decreased from 41.75% to 27.13% (Table 1), which coincided with previous findings that increasing the pyrolysis temperature accelerated the formation of syn-gas and bio-fuels and reduced biochar yield.<sup>24</sup> The yield of biochar is an important factor to evaluate its application as an adsorbent. Compared with cork-based biochar (28.37–24.26% yield from  $450^\circ\text{C}$  to  $750^\circ\text{C}$ ) and pristine banana pseudostem biochar (30.8% yield at  $400^\circ\text{C}$ , 25.1% at  $600^\circ\text{C}$ ), TBB had a higher yield at the identical pyrolysis temperature.<sup>8,25</sup>

### 3.2 Biochar characterization

**3.2.1 Physicochemical analysis.** The physicochemical properties of TBB were shown in Table 1. The results demonstrated that ash content in TBB800 was the highest among all the TBB, which was corroborated by the yield analysis. The ash contents were related to the presence of mineral elements in TB,

which increased at higher pyrolysis temperatures (additional information available in ESI†). In this work, TBB had lower ash contents compared to Jerusalem artichoke stalks biochar.<sup>26</sup> The pH value increased with increasing temperature, which resulted from the decomposition of acidic functional groups (e.g., carboxyl) and the formation of basic minerals in the pyrolysis

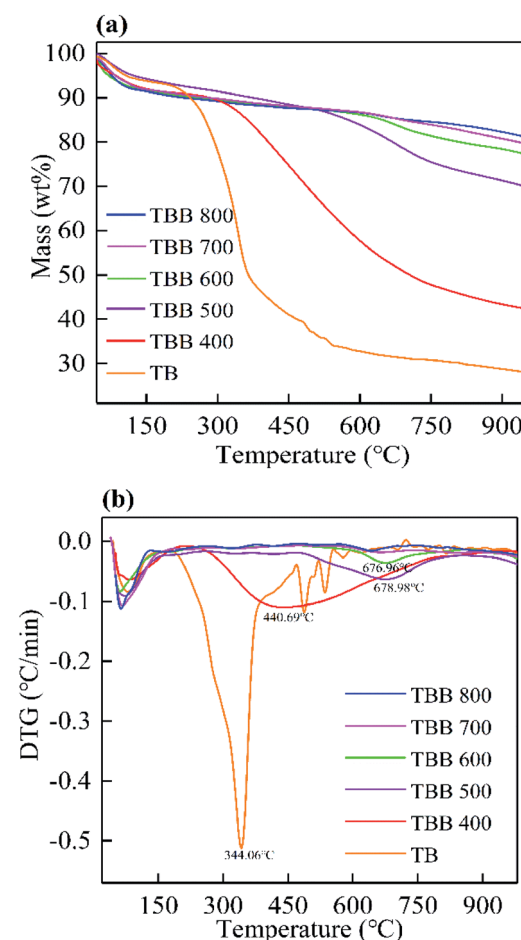


Fig. 1 TGA (a) and DTG (b) curves of TB and TBB.

Table 1 Characterization of TBB

Biochar	TBB400	TBB500	TBB600	TBB700	TBB800
Yield (%)	$41.75 \pm 0.59$	$35.27 \pm 0.86$	$32.63 \pm 0.41$	$31.89 \pm 0.72$	$27.13 \pm 0.51$
Ash (%)	$9.28 \pm 0.22$	$9.87 \pm 0.13$	$10.63 \pm 0.09$	$10.97 \pm 0.24$	$11.59 \pm 0.17$
pH	$8.45 \pm 0.01$	$8.63 \pm 0.01$	$8.72 \pm 0.02$	$8.87 \pm 0.01$	$9.81 \pm 0.01$
C (%)	61.11	67.09	70.45	73.08	79.66
H (%)	4.55	4.18	3.63	2.30	1.61
N (%)	1.85	1.52	1.36	1.00	0.71
O (%)	23.21	17.33	13.93	12.65	6.43
H/C	0.07	0.06	0.05	0.03	0.02
O/C	0.38	0.26	0.20	0.17	0.08
(N + O)/C	0.41	0.28	0.22	0.19	0.09
BET surface area ( $\text{m}^2 \text{ g}^{-1}$ )	5	8	180	277	208
Pore volume ( $\text{cm}^3 \text{ g}^{-1}$ )	0.05	0.07	0.09	0.12	0.11
Average pore diameter (nm)	5.43	4.84	4.43	2.36	2.18



process.<sup>27</sup> The C content increased from 61.11% to 79.66%, while the H, N, and O contents decreased with the increasing temperature, which resulted in a decrease in H/C, O/C, and (N + O)/C ratios. These trends were consistent with the previous researches.<sup>28</sup> The higher pyrolysis temperature led to the breaking of weak bonds, dehydration, and loss of oxygen-containing functional groups. Therefore, as the pyrolysis temperature increased, the degree of carbonization increased, and the surface of biochar had fewer polar functional groups and a more aromatic structure.

**3.2.2 Thermal gravimetric analysis.** Thermogravimetric analysis (TGA) and differential thermal analysis (DTG) were used to investigate the influence of pyrolysis temperature on TB and TBB (Fig. 1). As the pyrolysis temperature increased, biomass and biochar weight loss gradually decreased (Fig. 1a). The TGA of the TB curve was inverted S-shaped, and the total weight loss was 72.38% (at 950 °C). The pyrolysis process of TB was composed of three stages. The mass loss increased relatively slowly from 30 °C to 210 °C, mainly on account of the removal of bound water and other small molecular volatiles and residues.<sup>29</sup> At 210 to 470 °C, the mass of TB decreased sharply, and about 35% of the original mass remained due to the decomposition of most hemicellulose, cellulose, and less lignin.<sup>30</sup> At 470 to 950 °C, the weight loss became slower, ascribed to some lignin and extracts.<sup>31</sup> Consequently, these results showed that hemicellulose, cellulose, and lignin were the main components in TB, which were 12.11%, 16.82%, and 45.70% of feedstock, respectively. Furthermore, the weight loss of TBB400, TBB500, TBB600, TBB700, and TBB800 were 58.25%, 30.11%, 22.80%, 20.51%, and 18.90%, respectively.

Compared with TB, the DTG curves of TBB clearly showed that the peak value observed at 344.06 °C disappeared (Fig. 1b),

indicating that hemicellulose and cellulose decomposed at about 344 °C. However, lignin may still exist without degradation. The peak values of TBB400, TBB500, and TBB600 at 440.69, 678.98, and 676.96 °C were related to lignin, which would decompose between 400 and 750 °C. The curves of TBB700 and TBB800 were relatively stable. Most hemicellulose, cellulose, and lignin were decomposed in the pyrolysis process, indicating that TBB became more stable at higher temperature. These were consistent with the previous report.<sup>32</sup>

**3.2.3 BET and SEM analyses.** With the temperature increasing from 400 to 700 °C, the specific surface area and pore volume of TBB increased, which indicated that the pores in TBB developed gradually (Table 1). This may be due to the release of volatile compounds and the appearance of vascular bundle

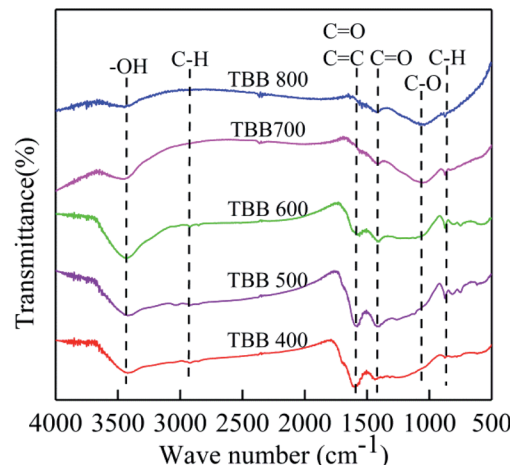


Fig. 3 FTIR spectra of TBB before Cd<sup>2+</sup> adsorption.

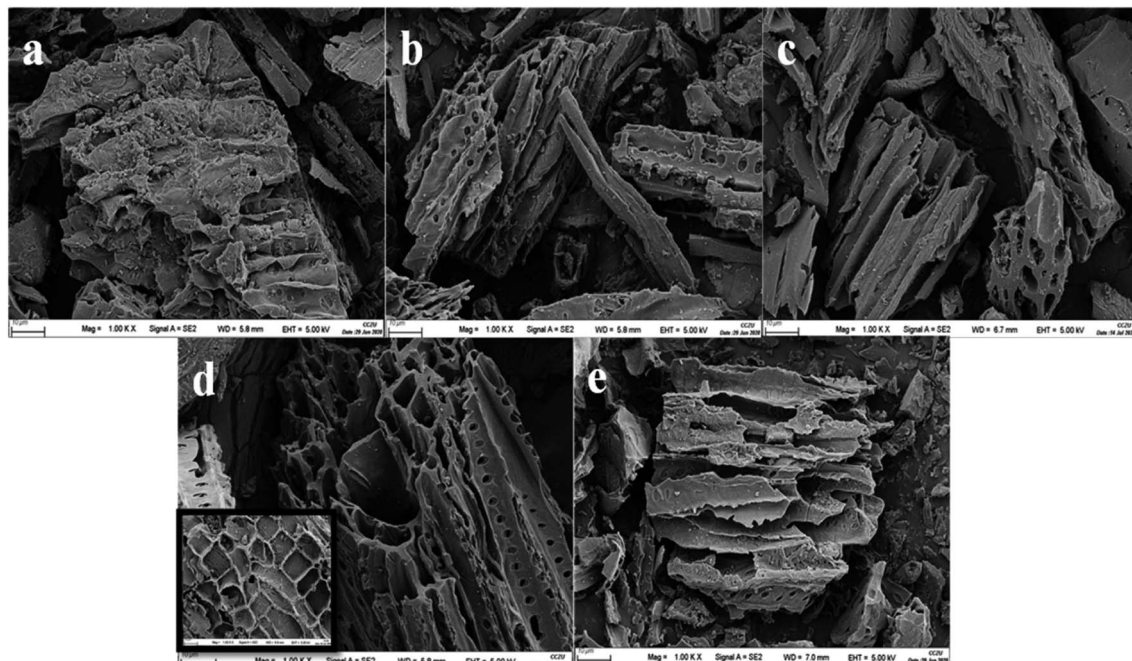
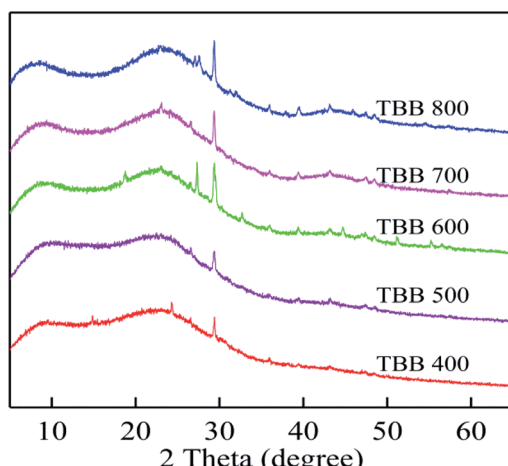


Fig. 2 SEM images of: (a) TBB400; (b) TBB500; (c) TBB600; (d) TBB700; (e) TBB800.



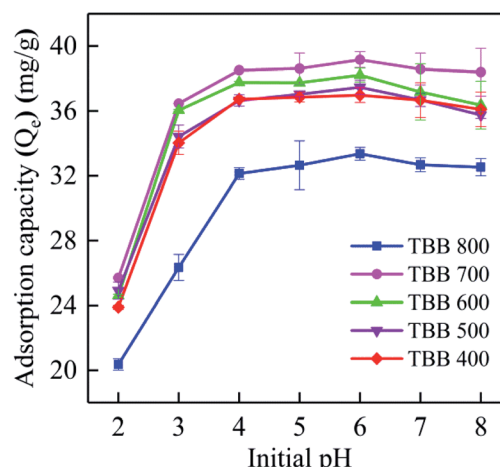
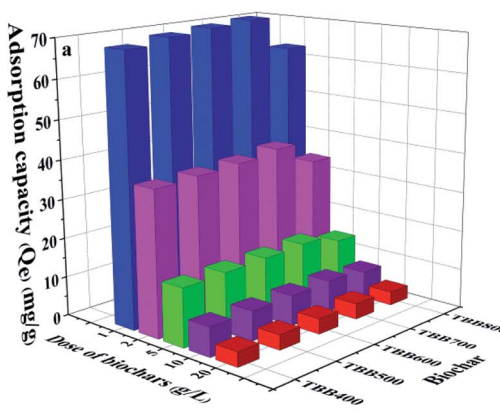
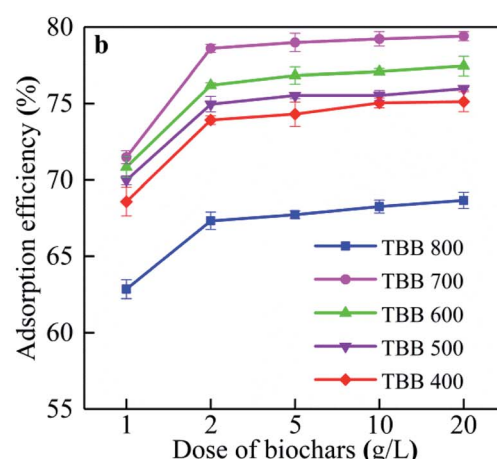
Fig. 4 XRD of TBB before  $\text{Cd}^{2+}$  adsorption.

structure after pyrolysis.<sup>28</sup> Compared with TBB400 and TBB500, the specific surface area of TBB600 increased sharply to  $180 \text{ m}^2 \text{ g}^{-1}$ , which corresponded to TGA. The high specific surface area was conducive to the adsorption of heavy metals by biochar. The degradation and destruction of cellulose brought about the formation of amorphous carbon structure and micropores below  $500^\circ\text{C}$ . The sharp increase in surface area from 500 to  $600^\circ\text{C}$  was attributed to the disintegration of lignin and the rapid release of  $\text{CH}_4$  and  $\text{H}_2$ , resulting in a massive micropore structure.<sup>24</sup> However, the specific surface area and pore volume decreased with increasing temperature at  $800^\circ\text{C}$ , which can be assumed to be transshaped or caving-in of microporous walls and thermal shrinkage of pores. A similar trend with the increasing pyrolysis temperature was found in the previous studies.<sup>33</sup> In the present study, the average pore size decreased due to more and more macropores transferred to meso and micro pores with the increasing temperature. The pores with the mesoporous structure were favorable for adsorption.

The SEM images showed the surface of TBB400 was rough, and the pore structure was not obvious (Fig. 2), which indicated

that the TB was not completely cracked and only partially carbonized. As the pyrolysis temperature increased, a deep pore structure with clear pores was found due to the gradual volatilization of organic matter and gas. These results indicated that the porous structure could be better developed at higher pyrolysis temperatures. The surface of TBB700 was tortoise shell-like, which provided more adsorption sites and favored the adsorption. The structural deformation and pore-clogging of TBB800 were due to the softening, melting, and fusion of limestone.<sup>34</sup> The porous structure was consistent with the above BET results.

**3.2.4 FTIR analysis.** The main intense bands were found at 3443, 2929, 1559, 1411, 1064, and  $801 \text{ cm}^{-1}$  from Fig. 3. With increasing pyrolysis temperature from 400 to  $800^\circ\text{C}$ , the decrease in band strength at  $3443 \text{ cm}^{-1}$  connected with  $-\text{OH}$  decreased, indicating that the dehydration reaction of cellulosic and ligneous components decreased gradually in TBB. This was one of the main reasons for the low polarity of biochar at high temperatures. The peaks at 2929 and  $801 \text{ cm}^{-1}$  correlated to the

Fig. 6 Effect of initial solution pH on the adsorption capacity of  $\text{Cd}^{2+}$  for TBB.Fig. 5 Effect of biochar dosage on adsorption capacity (a) and adsorption efficiency (b) of  $\text{Cd}^{2+}$  for TBB.

C–H bond were weak, and the peak at  $2929\text{ cm}^{-1}$  disappeared completely in TBB700. This may be due to the dehydration, demethylation, and demethoxylation of lignin, which brought about the reduction of aliphatic compounds as the temperature increased. When the temperature was higher than  $600\text{ }^\circ\text{C}$ , the

band at  $1559\text{ cm}^{-1}$  basically disappeared, which was connected with the skeletal vibrations of the C=C lignin absorption ring, and the carboxyl group decreased with dehydration and decarboxylation.<sup>35</sup> The absorption peak at  $1411\text{ cm}^{-1}$  connected with the C=O structure gradually weakened, indicating that the non-

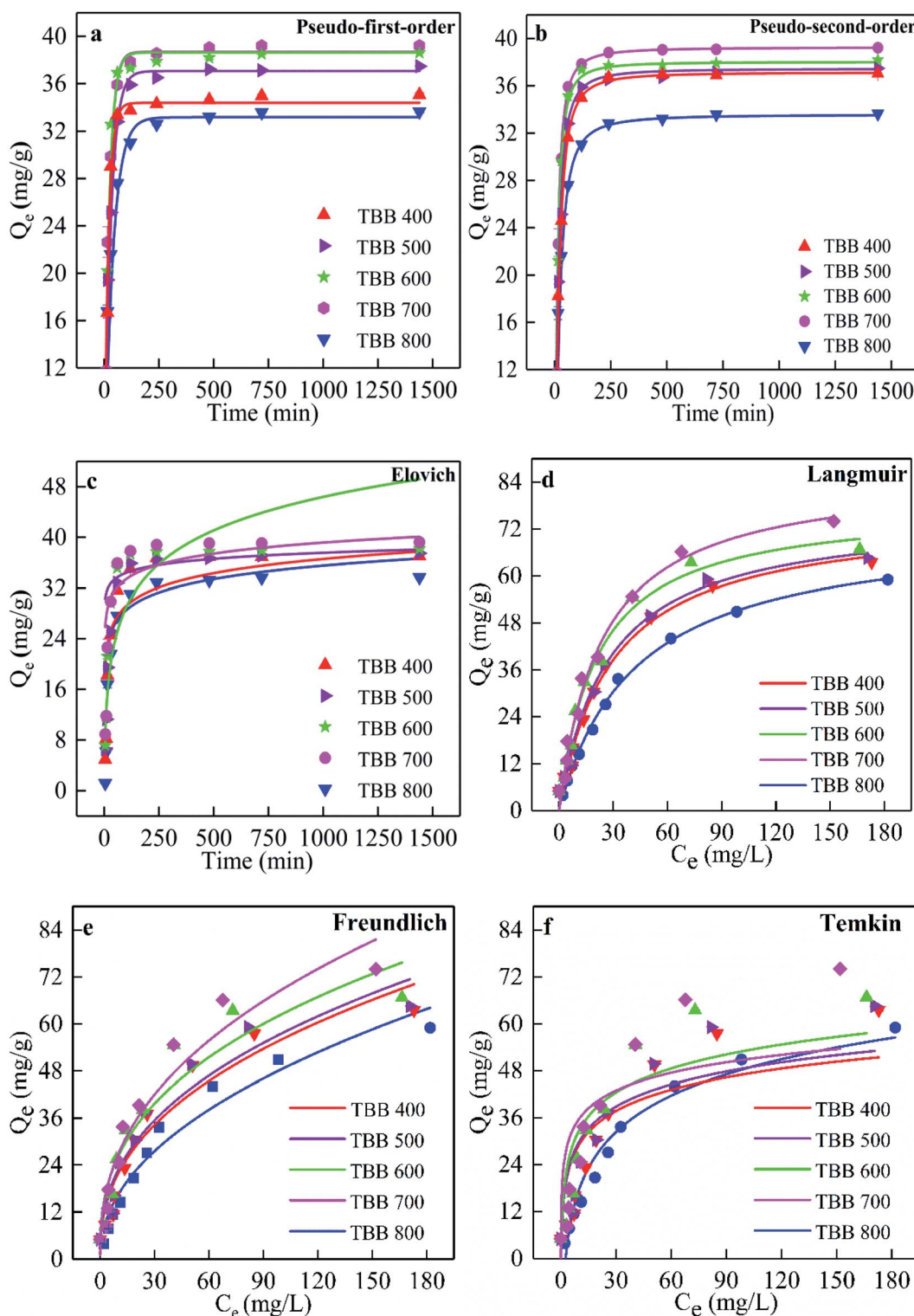


Fig. 7 Adsorption kinetics (a–c) and adsorption isotherms (d–f) of  $\text{Cd}^{2+}$  by TBB.

conjugate C=O structure in lignin has been decomposed.<sup>36</sup> Furthermore, new peaks appeared and strengthened at 1064 cm<sup>-1</sup> of TBB700 and TBB800, corresponding to the C=O stretching vibration of aromatic compounds.<sup>37</sup> These results clearly stated that the aromaticity of biochar was enhanced, and the carbon structure was more stable with the temperature increased, consistent with changes in element analysis and thermogravimetric analysis (Table 1 and Fig. 1).

**3.2.5 XRD analysis.** According to the XRD analysis (Fig. 4), the peak intensity and sharpness of  $2\theta$  at about 14.92° indicated the existence of amorphous and crystalline cellulose in TBB400. Nevertheless, the  $2\theta$  peak at 14.92° disappeared with the increase in temperature, indicating the decomposition of cellulose.<sup>38</sup> This was consistent with TGA (Fig. 1). All TBB presented a broad diffraction peak at 23–25°, attributing to the amorphous carbon property of TBB. Additionally, two peaks at  $2\theta$  of 27.18° and 29.28° belonged to the crystal structure of quartz and calcite, respectively.<sup>39</sup> The sharpness of the peak increased with increasing pyrolysis temperature from 400 to 800 °C, which was due to the relative decrease of the amorphous organic phase and the increase of ash percentage. This result was also consistent with elemental analysis (Table 1).

### 3.3 Effect of dosage and initial pH on Cd<sup>2+</sup> removal

The adsorption capacity per unit mass of TBB gradually decreased from 71.48–62.85 to 3.97–3.43 mg g<sup>-1</sup>, with the dosage ranging from 1 to 20 g L<sup>-1</sup> (Fig. 5a). With increased dosage, all the active sites cannot be completely occupied, which led to a transition of the surface from saturated to unsaturated and high adsorption capacity to low adsorption capacity.<sup>40</sup> There was no prominent change in the adsorption

efficiency of TBB when the dosage of biochar exceeds 2 g L<sup>-1</sup>, indicating that the adsorption sites of TBB and Cd<sup>2+</sup> reached a balance (Fig. 5b). Considering the adsorption capacity and adsorption efficiency of TBB, 2 g L<sup>-1</sup> was selected as the optimal dosage for the next experiment in this work.

The adsorption capacities of Cd<sup>2+</sup> on TBB were examined from pH 2 to 8, and it was observed that Cd<sup>2+</sup> could rapidly adsorb at pH 2–4. However, there was no significant effect at pH 5–8 (Fig. 6). According to the above FTIR analysis (Fig. 3), the TBB surface contains many hydroxyl (–OH) and carboxyl (–COOH) functional groups. At pH 2–4, a large number of hydrogen ions existed in the reaction system, which protonated the functional groups on the surface of TBB and repelled positively charged Cd<sup>2+</sup>.<sup>41</sup> Moreover, a high concentration of H<sup>+</sup> occupied the adsorption sites of Cd<sup>2+</sup> on the surface of TBB, resulting in low adsorption capacity.<sup>42</sup> When pH 5–8, the competitive adsorption capacity of TBB became weak due to the decrease in H<sup>+</sup>, and TBB can produce negatively charged functional groups, which generated high affinity for Cd<sup>2+</sup> to provoke Cd<sup>2+</sup> to dislodge from aqueous solution. At pH > 8, –OH and Cd<sup>2+</sup> formed the hydroxyl complex Cd(OH)<sub>2</sub>. When the initial solution pH was 6, the adsorption capacity of TBB was the highest. Hence the optimum pH was 6 in this experiment.

### 3.4 Analysis of adsorption kinetics

From Fig. 7a–c, the kinetic trend was composed of three stages: fast adsorption, slow adsorption, and equilibrium. The adsorption of Cd<sup>2+</sup> on TBB increased rapidly in the first 0.5 h, then tended to slow down, and gradually reached equilibrium after 4 h. TBB700 reached equilibrium faster and showed greater adsorption capacity than other TBB. Pseudo-second-

Table 2 Fitting parameters of kinetic models by TBB

Biochar	$Q_e^a$	Pseudo-first-order			Pseudo-second-order			Elovich		
		$Q_e$	$k_1$	$R^2$	$Q_e$	$k_2$	$R^2$	$\alpha$	$\beta$	$R^2$
TBB400	37.043	34.400	0.053	0.9302	37.127	0.010	0.9995	268.470	0.309	0.9025
TBB500	37.480	37.067	0.035	0.9667	37.442	0.015	0.9909	1.041	0.729	0.4483
TBB600	38.184	38.639	0.045	0.9767	38.024	0.020	0.9999	3.228	0.130	0.9058
TBB700	39.218	38.686	0.046	0.9757	39.251	0.027	0.9977	15 110.577	0.399	0.4936
TBB800	33.657	33.178	0.026	0.9592	33.578	0.009	0.9942	340.040	0.327	0.6382

<sup>a</sup> Actual adsorption capacity of TBB.

Table 3 Fitting parameters of isotherm models by TBB

Biochar	$T$ (°C)	Langmuir model			Freundlich model			Temkin		
		$Q_m$	$K_L$	$R^2$	$K_F$	$1/n$	$R^2$	$K_T$	$B$	$R^2$
TBB400	25	75.890	0.034	0.989	8.501	0.410	0.939	4.128	7.824	0.706
TBB500		76.189	0.037	0.986	8.967	0.404	0.939	3.827	8.181	0.722
TBB600		78.145	0.048	0.985	10.99	0.377	0.914	4.068	8.831	0.736
TBB700		86.548	0.043	0.986	10.41	0.410	0.937	22.736	6.577	0.584
TBB800		72.958	0.024	0.997	5.572	0.470	0.958	0.370	13.420	0.962



order  $R^2$  ( $R^2 > 0.99$ ) was greater than the pseudo-first-order and Elovich  $R^2$  (Table 2), which revealed that the pseudo-second-order model was more suitable for describing adsorption kinetics. This model can also be used to describe the adsorption kinetics of heavy metals on sewage sludge and barley straw biochar.<sup>7,15</sup> Furthermore, the adsorption value calculated by the pseudo-second-order approached the experimental value. These results further confirmed that the pseudo-second-order model was more suitable for describing adsorption kinetics, which meant that chemical adsorption was involved in the adsorption process.<sup>8,18</sup> Therefore, the adsorption mechanism of  $\text{Cd}^{2+}$  on TBB could be explained by two adsorption processes: physical adsorption and chemical adsorption, in which chemical adsorption dominated the reaction process.<sup>43</sup>

### 3.5 Adsorption isotherm analysis

The adsorption isotherm curves were shown in Fig. 7d-f. It was found that the adsorption capacity of TBB increased with the increased  $\text{Cd}^{2+}$  initial concentration and tended to be stable when the  $\text{Cd}^{2+}$  initial concentration reached  $100 \text{ mg L}^{-1}$ . In the whole process, the adsorption capacity of TBB700 was the highest, for which the maximum adsorption capacity fitted by the Langmuir isotherm model was  $86.55 \text{ mg g}^{-1}$ .

Langmuir, Freundlich, and Temkin isotherm models were adopted to interpret the adsorption equilibrium. The  $R^2$  of the Langmuir isotherm model was higher than that of others from Table 3, indicating that the adsorption of  $\text{Cd}^{2+}$  on the TBB surface was a homogeneous monolayer.<sup>44</sup> This result was in accordance with previous studies in KOH-modified rice straw and *Enteromorpha prolifera* biochar.<sup>14,45</sup> In this experiment,  $R_L$  was between 0.065 and 0.123, which further indicated that TBB has a great affinity for  $\text{Cd}^{2+}$ , and the adsorption process was favorable.<sup>46</sup> Meanwhile, when the Freundlich  $1/n$  parameter was between 0–1, the interactions between biochar and heavy metal ions were stronger. The  $1/n$  value of TBB was between 0.37–0.47.

Table 4 Comparison of maximum adsorption capacity of different biochars for  $\text{Cd}^{2+}$

Adsorbent	$Q_e^a$ ( $\text{mg g}^{-1}$ )	Reference
Peanut husk	28.99	10
Mango peel	13.28	11
Wheat straw	69.8	12
Corn stalk	40	47
Lotus seedpod-derived	51.18	48
Line tree residues	85.8	49
<i>Pleurotus ostreatus</i>	71.49	50
Shiitake substrate	46.87	
Buffalo weed	11.6	51
Rice straw	35.92	52
KOH-modified rice straw	41.9	14
KMnO <sub>4</sub> -modified vermicompost	60.23	15
Water hyacinth	70.3	58
TBB	74.04	This study

<sup>a</sup> Maximum adsorption capacity of the adsorbent.

in the present study, which further confirmed that the adsorption was favorable. The Temkin equation also fitted the adsorption data, indicating that the adsorption process of  $\text{Cd}^{2+}$  may be partly affected by the interaction between the adsorbent and adsorbate.

Many researchers have investigated the  $\text{Cd}^{2+}$  removal of biochar prepared from diverse raw materials. The superiority of TBB was assessed by comparing the  $\text{Cd}^{2+}$  adsorption capacity with other biochars reported in the literature. The results revealed that the maximum adsorption capacity of TBB700 used in this study was more efficient than most of the biochar and activated carbon reported in previous studies (Table 4). Consequently, the low cost, simplicity of production, and high adsorption capacity of TBB make it a promising alternative adsorbent for the treatment of  $\text{Cd}^{2+}$  contamination.

### 3.6 Reusability and stability

An acidic solution is often used to desorb the adsorbent after heavy metal adsorption. The regeneration and reusability of TBB700 were investigated to evaluate the potential applicability.

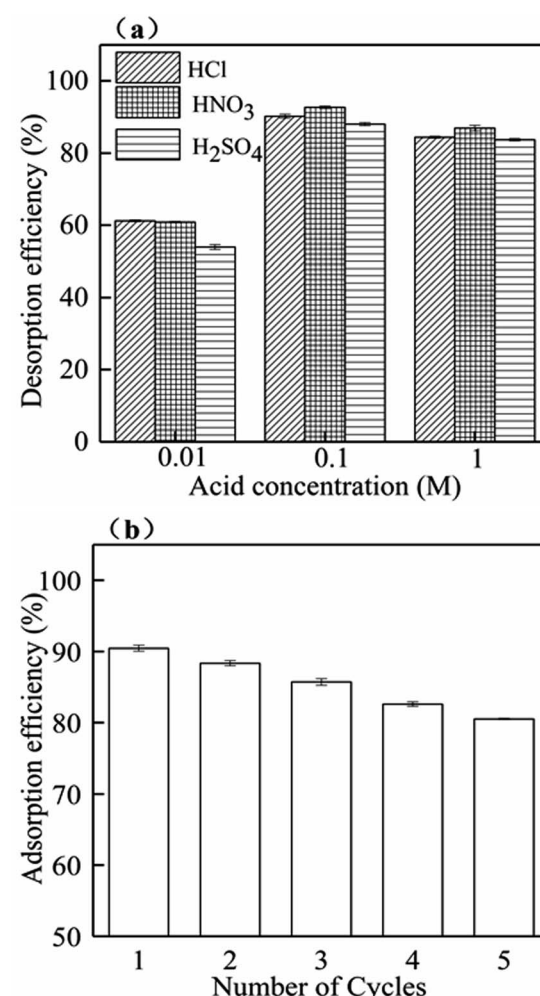


Fig. 8 Effect of desorption agent concentration on  $\text{Cd}^{2+}$  desorption (a) and recycling adsorption efficiency of  $\text{Cd}^{2+}$  for TBB700 (b).



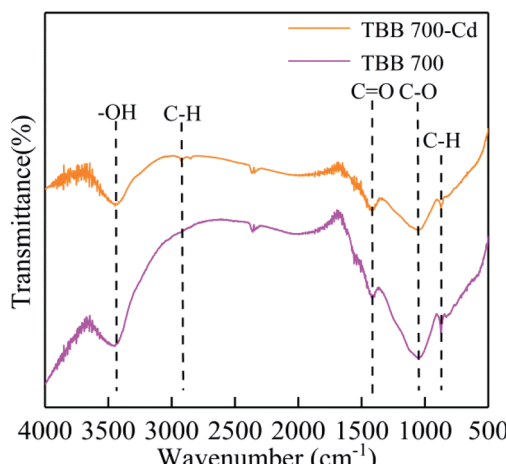


Fig. 9 FTIR spectra of TBB700 before and after  $\text{Cd}^{2+}$  adsorption.

The desorption efficiency of 0.1 M acid solution was higher than that of 0.01 and 1 M, and  $\text{HNO}_3$  had high desorption efficiency compared with  $\text{HCl}$  and  $\text{H}_2\text{SO}_4$  (Fig. 8a). So, 0.1 M  $\text{HNO}_3$  can be used as the best desorption agent. After five cycles of desorption–adsorption experiments, the adsorption capacity slightly decreased. However, the adsorption rate remained above 80% (Fig. 8b). The decreasing adsorption rate may be thanks to partial saturation of surface active sites or exhaustion of surface functional groups. Therefore, TBB showed good reproducibility, stability, and reusability for removing  $\text{Cd}^{2+}$  from wastewater.

### 3.7 Mechanism of $\text{Cd}^{2+}$ adsorption

According to the adsorption kinetics and isotherm, it was shown that the adsorption of TBB was mainly monolayer chemical adsorption, and the TBB surface had a homogeneous structure. The adsorption mechanism of TBB700 before and after  $\text{Cd}^{2+}$  adsorption was further analyzed by FTIR, SEM elemental mapping, XRD, and XPS. The functional groups of TBB700 changed significantly before and after  $\text{Cd}^{2+}$  adsorption (Fig. 9). After adsorption, the  $-\text{OH}$  peak shifted from 3443 to  $3448\text{ cm}^{-1}$  and the intensity decreased, which was mostly consumed in the adsorption process of  $\text{Cd}^{2+}$  to form  $\text{Cd}-\text{O}$  complexes or the deposits of  $\text{Cd}(\text{OH})_2$  on the TBB surface. This result was consistent with the studies in pinecone and  $\text{KMnO}_4$ -modified vermicompost biochar.<sup>15,18</sup> However, it was different

Table 5 Elemental mass percentage of TBB700 before and after  $\text{Cd}^{2+}$  adsorption

Element	Weight (%)	
	Before	After
C	76.62	79.78
O	17.26	15.02
K	2.91	1.41
Ca	1.78	0.67
Na	0.37	0.13
Mg	1.06	0.59
Cd	0	2.4
Total	100	100

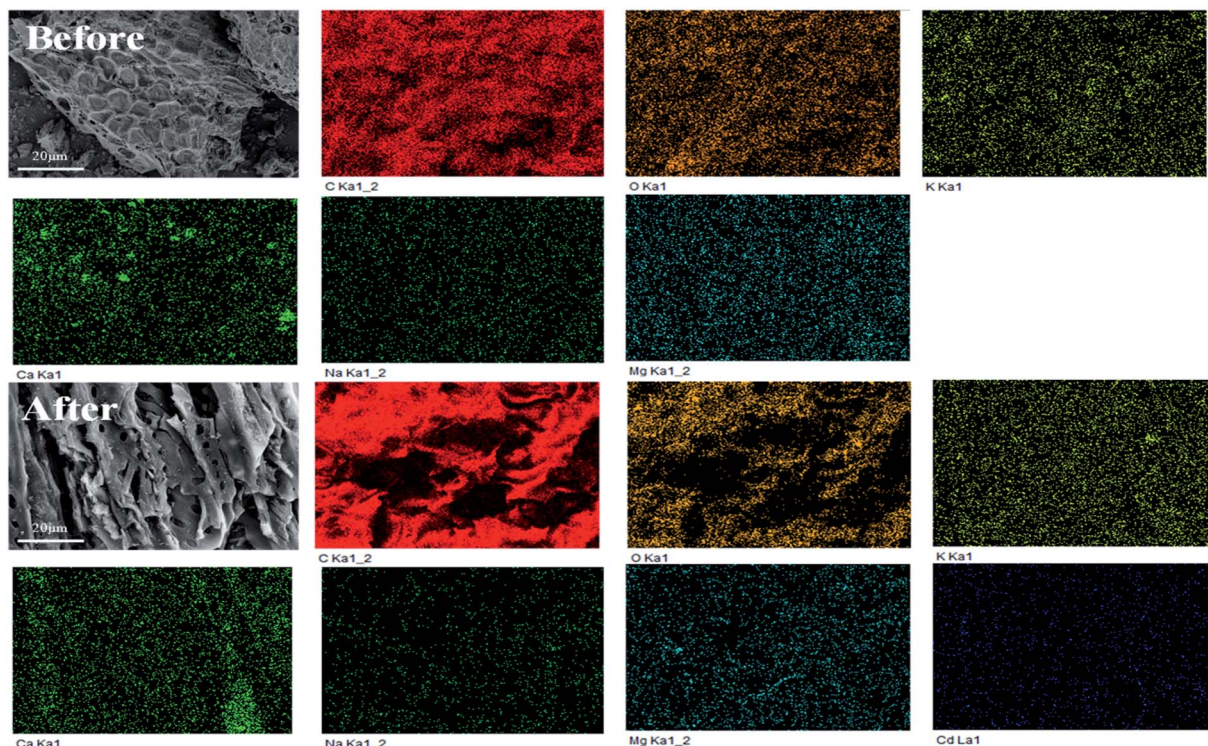


Fig. 10 SEM elemental mapping of TBB700 before and after  $\text{Cd}^{2+}$  adsorption.



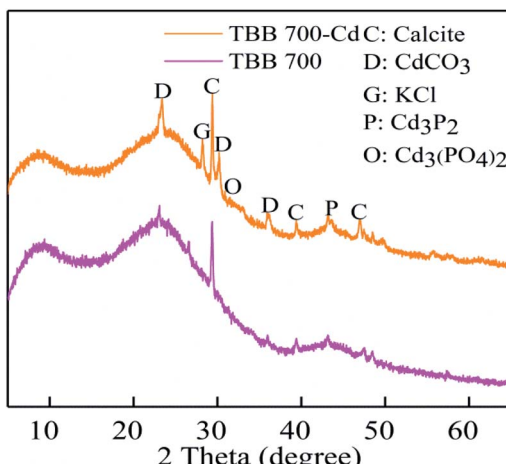


Fig. 11 XRD of TBB700 before and after  $\text{Cd}^{2+}$  adsorption.

from the results observed by Li *et al.*, who observed that the intensity of the peak increased after adsorption because of the dissociation of hydroxyl ions during anion exchange.<sup>53</sup> The intensity of peaks at  $1411$  and  $1064\text{ cm}^{-1}$  associated with  $\text{CO}_3^{2-}$  and  $\text{PO}_4^{3-}$ , respectively, weakened and disappeared after  $\text{Cd}^{2+}$  adsorption, directly confirming that surface  $\text{CO}_3^{2-}$  and  $\text{PO}_4^{3-}$  groups played an important role in the removal of  $\text{Cd}^{2+}$  by precipitation.<sup>14,54</sup> Furthermore, compared with those before

$\text{Cd}^{2+}$  adsorption, the peaks in the bands of  $3200$ – $2800$  and  $801\text{ cm}^{-1}$  correlated to the C–H stretching increased and decreased, respectively. The changes in peak position and peak strength indicated that C–O, C=O, and C–H groups participated in the complexation reaction during  $\text{Cd}^{2+}$  adsorption, in which C–O and C=O were the main functional groups for  $\text{Cd}^{2+}$  removal on the surface of TBB.

Metal ion exchange and surface precipitation play a significant role in heavy metal removal.<sup>17,55</sup> The elements on the surface of TBB were mainly C, O, K, Ca, Na, Mg, and Cd, which confirmed the binding of  $\text{Cd}^{2+}$  to TBB (Fig. 10 and Table 5). The mass percentage of K, Ca, Na, and Mg decreased after adsorption, which meant that these cations were substituted by  $\text{Cd}^{2+}$  and released from the surface of TBB. According to the XRD analysis of TBB700 before and after  $\text{Cd}^{2+}$  adsorption (Fig. 11), it was observed that the peak of  $23.36^\circ$  became sharper, and new peaks appeared at  $30.10^\circ$  and  $35.92^\circ$  in TBB700-Cd, which indicated that  $\text{CdCO}_3$  was deposited on the surface of TBB700.<sup>14,56</sup> At the same time, a small amount of  $\text{Cd}_3\text{P}_2$  and  $\text{Cd}_3(\text{PO}_4)_2$  precipitates were also produced, which was consistent with FTIR analysis.<sup>57,58</sup> The adsorption mechanism of  $\text{Cd}^{2+}$  by TBB700 was specific adsorption in the form of ion exchange and hydroxyl binding. Besides, K, Ca, Na, Mg, and P contents increased with the increase in pyrolysis temperature, which was conducive to metal ion exchange and surface precipitation (additional information available in ESI†).

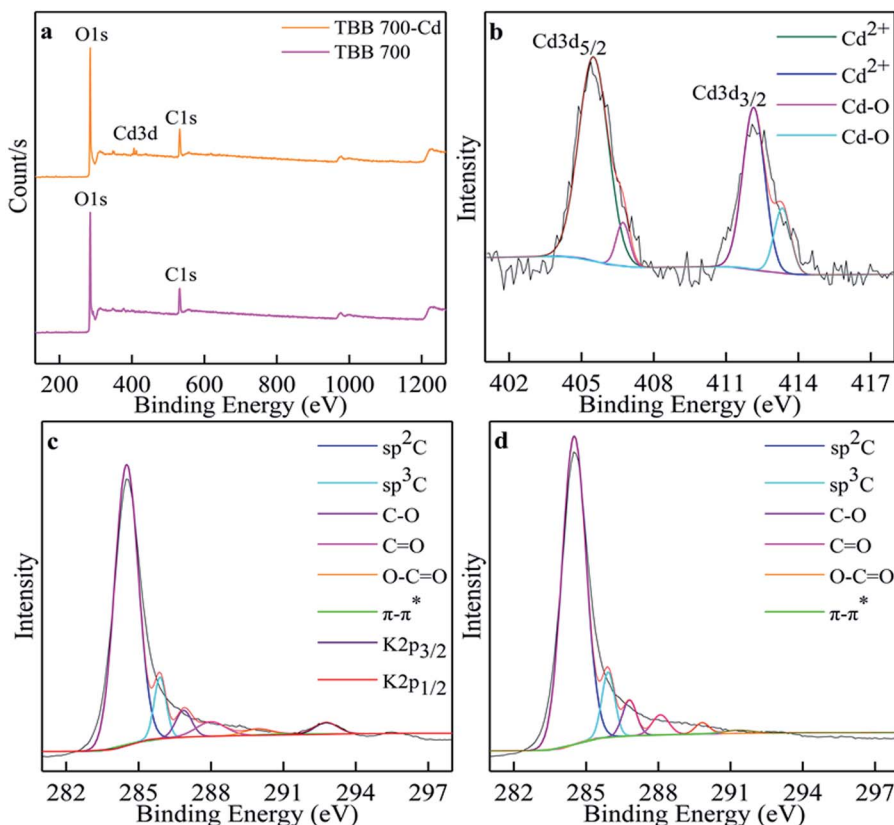


Fig. 12 XPS of TBB700 before and after  $\text{Cd}^{2+}$  adsorption (a); Cd 3d for TBB700 after  $\text{Cd}^{2+}$  adsorption (b); C1s for TBB700 before (c) and after (d)  $\text{Cd}^{2+}$  adsorption.



XPS analysis further investigated the composition and valence states of elements on the surface of TBB700 at the micro level before and after adsorption in order to detect the immobilization mechanism of Cd<sup>2+</sup>. Cd3d peak appeared at 406.08 eV in the XPS spectrum after adsorption of Cd<sup>2+</sup> (Fig. 12a), which further revealed that Cd<sup>2+</sup> was found on the surface of TBB700. Spectra of Cd3d exhibited Cd3d<sub>5/2</sub> and Cd3d<sub>3/2</sub> peaks located at 405.50 and 412.15 eV, indicating Cd<sup>2+</sup> was combined to the TBB700 in the form of CdCO<sub>3</sub>, and Cd–O/Cd(OH)<sub>2</sub> bonds at 406.72 and 413.33 eV (Fig. 12b). The peaks at 405.50 and 412.15 eV indicated that Cd<sup>2+</sup> was complexed with deprotonated form (–O<sup>–</sup>) or hydroxyl (–OH) on the TBB as well.<sup>15,59</sup> The high-resolution C1s spectrum was decomposed into eight peaks (Fig. 12c). The binding energies of 284.49, 285.89, 286.87, 287.99, and 289.95 eV were distributed on sp<sup>2</sup>C, sp<sup>3</sup>C, C–O, C=O/C–O–C, and O–C=O, respectively. The binding of 291.42 eV can be traced to the  $\pi$ – $\pi^*$  transition, which is characteristic of conjugated or aromatic systems.<sup>15,60</sup> As an electron-rich aromatic  $\pi$  donor, TBB700 could interact with Cd<sup>2+</sup> as a  $\pi$  receptor. The binding energies of 292.78 and 295.76 eV could have a bearing on K2p<sub>3/2</sub> and K2p<sub>1/2</sub>, respectively. As shown in Fig. 12d, after Cd<sup>2+</sup> adsorption, the C–O shifted slightly from 286.87 to 286.80 eV, and the O–C=O shifted slightly from 289.95 to 289.82 eV, indicating that the adsorption of Cd<sup>2+</sup> by TBB involves –OH and –COOH. The release of potassium ions from the surface of biochar brings about the vanishing of the potassium peak, which indicates the ion exchange between cadmium and potassium ions. This was consistent with the results of SEM element mapping (Fig. 10 and Table 5).

## 4. Conclusion

Until now, there have been no studies on the production of biochar derived from TB and its application for Cd<sup>2+</sup> removal from aqueous media. In this study, TBB700 exhibited outstanding surface properties, high adsorption capacity, excellent reusability, and stability after five cycles of adsorption. The adsorption mechanism of TBB mainly included surface complexation, precipitation, metal ion exchange, and Cd<sup>2+</sup>– $\pi$  interaction. Overall, this study showed that TBB700 was an environmentally friendly, effective, and low-cost sorbent for the treatment of Cd<sup>2+</sup> contaminated water.

## Conflicts of interest

There are no conflicts to declare.

## Acknowledgements

This work was supported by the National Natural Science Foundation of China (31460100 and 31660477), Postgraduate Research & Practice Innovation Program of Jiangsu Province (SJCX21-1186 and SJCX21-1187), and National College Students Innovation and Entrepreneurship Training Program of Jiangsu Province (2020-C-03).

## References

- X. Cui, H. Hao, C. Zhang, Z. He and X. Yang, *Sci. Total Environ.*, 2016, **539**, 566–575.
- Y. Asci, M. Nurbas and Y. S. Acikel, *J. Hazard. Mater.*, 2008, **154**, 663–673.
- X. Gong, D. Huang, Y. Liu, Z. Peng, G. Zeng, P. Xu, M. Cheng, R. Wang and J. Wan, *Crit. Rev. Biotechnol.*, 2018, **38**, 455–468.
- J. He, Y. Ren, X. Chen and H. Chen, *Ecotoxicol. Environ. Saf.*, 2014, **108**, 114–119.
- G. Z. Kyzas, B. George, R. I. Kosheleva, E. K. Efthimiadou, E. P. Favvas, K. Margaritis and A. C. Mitropoulos, *Chem. Eng. J.*, 2018, **356**, 91–97.
- M. Bilal, J. A. Shah, T. Ashfaq, S. Gardazi, A. A. Tahir, A. Pervez, H. Haroon and Q. Mahmood, *J. Hazard. Mater.*, 2013, **263**, 322–333.
- R. Jazini, M. Soleimani and N. Mirghaffari, *Water Environ. J.*, 2018, **32**, 125–133.
- Q. H. Wang, Z. Y. Lai, J. Mu, D. M. Chu and X. R. Zang, *Waste Manag.*, 2020, **105**, 102–109.
- R. Li, H. Deng, X. Zhang, J. J. Wang and Z. Zhang, *Bioresour. Technol.*, 2018, **273**, 335–340.
- Q. M. Cheng, Q. Huang, S. Khan, Y. J. Liu, Z. N. Liao, G. Li and Y. S. Ok, *Ecol. Eng.*, 2016, **87**, 240–245.
- L. M. Zhang, Y. F. Ren, Y. H. Xue, Z. W. Cui, Q. H. Wei, C. Han and J. Y. He, *RSC Adv.*, 2020, **10**, 35878–35888.
- L. Liu and S. S. Fan, *Environ. Sci. Pollut. Res.*, 2018, **25**, 8688–8700.
- S. Y. Yoon, S. B. Jang, K. T. Wong, H. Kim, M. J. Kim, C. E. Choong, J. Yang, Y. Y. Chang, S. E. Oh, Y. Yoon and M. Jang, *J. Hazard. Mater.*, 2021, **417**, 125995.
- S. Bashir, J. Zhu, Q. L. Fu and H. Q. Hu, *Environ. Sci. Pollut. Res.*, 2018, **25**, 11875–11883.
- J. Z. Zhang, X. F. Ma, L. Yuan and D. X. Zhou, *J. Environ. Manage.*, 2020, **256**, 109959.
- S. Fan, H. Li, Y. Wang, Z. Wang, J. Tang, J. Tang and X. Li, *Res. Chem. Intermed.*, 2018, **44**, 135–154.
- Y. F. Jia and K. M. Thomas, *Langmuir*, 2000, **16**, 1114–1122.
- D. Teng, B. Zhang, G. Xu, B. Wang, K. Mao, J. Wang, J. Sun, X. Feng, Z. Yang and H. Zhang, *Environ. Pollut.*, 2020, **265**, 115001.
- F. Huang, L. Y. Gao, R. R. Wu, H. Wang and R. B. Xiao, *Sci. Total Environ.*, 2020, **731**, 139–163.
- R. Z. Wang, D. L. Huang, Y. G. Liu, C. Zhang, C. Lai, G. M. Zeng, M. Cheng, X. M. Gong, J. Wan and H. Luo, *Bioresour. Technol.*, 2018, **261**, 265–271.
- S. H. Lee, T. V. Doherty, R. J. Linhardt and J. S. Dordick, *Biotechnol. Bioeng.*, 2009, **102**, 1368–1376.
- J. Rouquerol, P. Llewellyn and F. Rouquerol, *Stud. Surf. Sci. Catal.*, 2007, **160**, 49–56.
- S. Brandani, *Adsorption*, 2021, **27**, 353–368.
- B. Zhao, D. O'Connor, J. L. Zhang, T. Y. Peng, Z. T. Shen, D. C. W. Tsang and D. Y. Hou, *J. Cleaner Prod.*, 2018, **174**, 977–987.
- S. Liu, J. H. Li, S. Xu, M. Z. Wang, Y. C. Zhang and X. H. Xue, *Bioresour. Technol.*, 2019, **282**, 48–55.



26 J. Wei, C. Tu, G. Yuan, Y. Liu, D. Bi, L. Xiao, J. Lu, B. K. G. Theng, H. Wang and L. Zhang, *Environ. Pollut.*, 2019, **251**, 56–65.

27 M. Ahmad, S. S. Lee, X. M. Dou, D. Mohan, J. K. Sung, J. E. Yang and Y. S. Ok, *Bioresour. Technol.*, 2012, **118**, 536–544.

28 W. K. Kim, T. Shim, Y. S. Kim, S. Hyun, C. Ryu, Y. K. Park and J. Jung, *Bioresour. Technol.*, 2013, **138**, 266–270.

29 K. M. Jiang, C. G. Cheng, M. Ran, Y. G. Lu and Q. L. Wu, *New Carbon Mater.*, 2018, **33**, 183–187.

30 S. K. Bhatia, R. Gurav, T. R. Choi, H. J. Kim, S. Y. Yang, H. S. Song, J. Y. Park, Y. L. Park, Y. H. Han, Y. K. Choi, S. H. Kim, J. J. Yoon and Y. H. Yang, *Bioresour. Technol.*, 2020, **302**, 122872.

31 K. H. Kim, J. Y. Kim, T. S. Cho and J. W. Choi, *Bioresour. Technol.*, 2012, **118**, 158–162.

32 W. J. Liu, H. Jiang and H. Q. Yu, *Chem. Rev.*, 2015, **115**, 12251–12285.

33 D. Angin, *Bioresour. Technol.*, 2013, **128**, 593–597.

34 I. D. Manariotis, K. N. Fotopoulou and H. K. Karapanagioti, *Ind. Eng. Chem. Res.*, 2015, **54**, 9577–9584.

35 L. Wei, S. Liang, N. M. Guho, A. J. Hanson, M. W. Smith, M. Garcia-Perez and A. G. McDonald, *J. Anal. Appl. Pyrolysis*, 2015, **115**, 268–278.

36 B. B. Uzun, E. Apaydin-Varol, F. Ates, N. Ozbay and A. E. Putun, *Fuel*, 2010, **89**, 176–184.

37 R. Karunanithi, Y. S. Ok, R. Dharmarajan, M. Ahmad, B. Seshadri, N. Bolan and R. Naidu, *Environ. Technol. Innovation*, 2017, **8**, 113–125.

38 Z. Wang, J. Cao and J. Wang, *J. Anal. Appl. Pyrolysis*, 2009, **84**, 179–184.

39 X. He, Z. N. Hong, J. Jiang, G. Dong, H. Liu and R. K. Xu, *Environ. Sci. Pollut. Res.*, 2021, DOI: 10.1007/s11356-021-13742-8.

40 J. Zhang and P. Zheng, *RSC Adv.*, 2015, **5**, 17768–17774.

41 X. L. Dong, L. Q. Ma, J. Gress, W. Harris and Y. C. Li, *J. Hazard. Mater.*, 2014, **267**, 62–70.

42 Z. W. Cui, Y. F. Ren, W. Wang, L. M. Zhang, L. Y. Zhang, X. Y. Wang and J. Y. He, *Environ. Sci.*, 2020, **41**, 3315–3325.

43 X. Huang, N. Y. Gao and Q. L. Zhang, *J. Environ. Sci.*, 2007, **19**, 1287–1292.

44 P. Z. Zhang, Y. F. Li, Y. Y. Cao and L. J. Han, *Bioresour. Technol.*, 2019, **285**, 121348.

45 K. L. Qiao, W. J. Tian, J. Bai, J. Dong, J. Zhao, X. X. Gong and S. H. Liu, *Ecotoxicol. Environ. Saf.*, 2018, **149**, 80–87.

46 F. Reguyal, A. K. Sarmah and W. Gao, *J. Hazard. Mater.*, 2017, **321**, 868–878.

47 G. Y. Chen, C. B. Wang, J. N. Tian, J. P. Liu, Q. J. Ma, B. Liu and X. P. Li, *J. Water Process. Eng.*, 2020, **35**, 101223.

48 Z. Chen, T. Liu, J. J. Tang, Z. J. Zheng, H. M. Wang, Q. Shao, G. L. Chen, Z. X. Li, Y. Q. Chen, J. W. Zhu and T. Feng, *Environ. Sci. Pollut. Res.*, 2018, **25**, 11854–11866.

49 J. H. Park, J. J. Wang, S. H. Kim, S. W. Kang, C. Y. Jeong, J. R. Jeon, K. H. Park, J. S. Cho, R. D. Delaune and D. C. Seo, *J. Colloid Interface Sci.*, 2019, **553**, 298–307.

50 Y. Xian, J. Wu, G. Yang, R. Liao, X. Zhang, H. Peng, X. Yu, F. Shen, L. Li and L. Wang, *RSC Adv.*, 2018, **8**, 28002–28012.

51 K. Yakkala, M. R. Yu, H. Roh, J. K. Yang and Y. Y. Chang, *Desalin. Water Treat.*, 2013, **51**, 7732–7745.

52 X. Han, C. F. Liang, T. Q. Li, K. Wang, H. G. Huang and X. E. Yang, *J. Zhejiang Univ., Sci., B*, 2013, **7**, 640–649.

53 H. Li, Y. Yang, S. Yang, A. Chen and D. Yang, *J. Spectrosc.*, 2014, **2014**, 671956.

54 X. D. Cao and W. Harris, *Bioresour. Technol.*, 2010, **101**, 5222–5228.

55 L. Trakal, V. Veselska, I. Safarik, M. Vitkova, S. Cihalova and M. Komarek, *Bioresour. Technol.*, 2016, **203**, 318–324.

56 F. Zhang, X. Wang, D. X. Yin, B. Peng, C. Y. Tan, Y. G. Liu, X. F. Tan and S. X. Wu, *J. Environ. Manage.*, 2015, **153**, 68–73.

57 G. C. Tan, W. L. Sun, Y. R. Xu, H. Y. Wang and N. Xu, *Bioresour. Technol.*, 2016, **211**, 727–735.

58 H. Wang, B. Gao, S. Wang, J. Fang, Y. Xue and K. Yang, *Bioresour. Technol.*, 2015, **197**, 356–362.

59 G. Q. Tan and D. Xiao, *J. Hazard. Mater.*, 2009, **164**, 1359–1363.

60 X. Hu, Z. Ding, A. R. Zimmerman, S. Wang and B. Gao, *Water Res.*, 2015, **68**, 206–216.

